Geomechanics and Engineering, *Vol. 25, No. 3 (2021) 253-266*
DOI: https://doi.org/10.12989/gae.2021.25.3.253

The new approach to calculate pulse wave returning energy vs. mechanical energy of rock specimen in triaxial test

Mojtaba Heidari[1a], Rassoul Ajalloeian[*1], Akbar Ghazi Fard[1] and Mahmoud Hashemi Isfahanian[2]

[1]Department of Geology, University of Isfahan, Isfahan, Hezar-Jarib Avenue, Islamic Republic of Iran
[2]Department of Civil Engineering and Transportation, University of Isfahan, Isfahan, Hezar Jirib Avenue, Islamic Republic of Iran

(Received June 26, 2019, Revised April 14, 2021, Accepted April 26, 2021)

Abstract. In this paper, we discuss a mathematical method for determining the return energy of the wave from the sample and comparing it with the mechanical energy consumed to change the dimension of the sample in the triaxial test of the rock. We represent a method to determine the mechanical energy and then we provide how to calculate the return energy of the wave. However, the static energy and pulse return energy will show higher amounts with axial pressure increase.
Three types of clastic sedimentary rocks including sandstone, pyroclastic rock, and argillitic tuff were selected. The sandstone showed the highest strength, Young's modulus and ultrasonic P and S waves' velocities versus others in the triaxial test. Also, from the received P wavelet, the calculated pulse wave returning energy indicated the best correlation between axial stress compared to wave velocities in all specimens. The fact that the return energy decreases or increases is related to increasing lateral stress and depends on the geological characteristics of the rock. This method can be used to determine the stresses on the rock as well as its in-situ modulus in projects that are located at high depths of the earth.

Keywords: return energy of the wave; triaxial test; sedimentary rocks; pyroclastic rock; ultrasonic wave velocities

1. Introduction

The construction of deep structures such as tunnels depends on geological conditions and the environments that surround them along with the mechanical properties of rocks. Descriptions of rock strength and deformational behavior are fundamental to evaluate the stability of engineering structures located in rock (Xie 2009). The ultimate strength of Young's modulus of rocks are not adequate parameters for judgments of stress-strain behavior.

The stress-strain behavior of rocks depends on rock type, physical and mechanical properties of rocks, homogeneity and isotropy of it, type of test for determining stress-strain relationships of rocks, and details of test and machine used for conducting the test. Triaxial test of rock can show the behavior of rock during loading incomplete state that contains elastic, plastic, failure, and even post-failure. Stress-strain relationships of rocks in this test are generally nonlinear. Brittle rocks have elastic behavior and ductile rocks have elastic mode at the beginning loading stage and plastic behavior at the next stage.

Many factors can affect the behavior types of rocks in the triaxial test. For example, loading rate, moisture content, temperature, and lateral pressure applied to the sample have a significant impact on it.

The amount of deformation in the loading process is defined by Young's modulus and can be determined from static and dynamic methods. In the static method, the surface under the stress-strain curve determines energy or work. Also, the stress-strain slope line shows Young's modulus of elasticity in the static method.

In the dynamic method, usually, the velocity of the ultrasonic pulse wave in rocks can determine the properties of rocks. Acoustic emission (AE) event counts, AE count rates scaled with the stress-strain relationship, the source location of the events, maximum amplitude, attenuation of AE, etc. are recently used by researchers to study the rock deformation mechanism and characteristics under different loading conditions until failure and also post-failure (Martinez-Martinez *et al.* 2012, Najibi *et al.* 2015 and Li *et al.* 2019).

Ultrasonic waves are a good index for evaluating the change of internal structure and mechanical properties of rocks. When the elastic wave encounters certain obstacles during propagation, such as inclusions, holes, and cracks, ultrasonic attenuation will occur. This process is presented by the decline of ultrasonic wave velocity or amplitude (Lu and Wu 2016). Fereidooni (2018) has evaluated the effects of mineral content and porosity on ultrasonic wave velocity.

Amplitude distributions of AE signals have been used to infer the relationship between variations of AE event magnitudes and failure processes of rocks (Sun *et al.* 1991). He *et al.* (2010) have correlated the frequency–amplitude of AE signals with the rockburst behaviors. Kong *et al.* (2018) has studied cracks evolution and multifractal of acoustic emission energy in coal rock during the uniaxial compression test.

Zhao *et al.* (2013) determined the crack initiation stress

---

*Corresponding author, Professor
E-mail: rasajl@sci.ui.ac.ir
[a]Ph.D.
E-mail: heidari@sci.ui.ac.ir, engheidari@gmail.com

http://www.techno-press.org/?journal=gae&subpage=7

ISSN: 2005-307X (Print), 2092-6219 (Online)

(σ_{ci}) and crack damage stress (σ_{cd}) with AE parameters such as ringdown counts, energy, and event duration in uniaxial and triaxial tests.

In this article, another Acoustic Emission (AE) parameters of waves, the energy receiving from ultrasonic sending wave in rock sample during triaxial test calculated too. The rock deformations process under axial and lateral stresses are associated with changes in acoustic emission (AE) parameters. AE is a transient elastic wave that is generated by the rapid release of energy within a material (Koerner *et al.* 1981 and Lockner 1993). For calculation of returned pulse energy, all wavelet surface between the neutral horizontal axis after receiving until attenuation must be calculated.

In this research, the convenient parameters that are registered from a complete triaxial test of rock are determined, and also wave energy that is received from ultrasonic wavelet is calculated and compared with static energy that is consumed for the transformation of the specimen. Rock strength and its deformations under stress are the most important factors for the design of engineering constructions. But the determination of these parameters usually obtained from destructive methods. Also, the results have useful data for the assessment of tectonic activities in the active zone and the prediction of rock behavior at in situ stress.

Due to high sensitivity to compression, crack initiation, propagation, and coalescence in rocks subjected to loading, the non-destructive and dynamic real-time monitoring method provides a powerful tool for investigating brittle rock failure and this technique has been widely used in rock mechanics studies and engineering applications (Mlakar *et al.* 1994, Chang and Lee 2004, Cai *et al.* 2007, Moradian *et al.* 2010 and Zhao *et al.* 2013).

Although many studies are conducted on the physical and dynamical properties of rocks under stress, they are mainly focused on either the variation of deformability, ultrasonic velocity, or AE activity separately. Besides, because of the limitations of testing equipment, they mostly did not concentrate on wave energy obtained from P and S wavelets.

In this study, an experimental test of the ultrasonic wave to return wave energy, which was used to study the deformation behavior of the sample under triaxial loading was developed. Also, the results of static rock deformation, P-wave velocity, S-wave velocity, and P-wave return wave energy were recorded and analyzed. Finally, the deformation process and evaluation of static and dynamic parameters especially the energy of them were evaluated.

The results provide new insights into the best comparison between static and dynamic energy of rock during the triaxial test and lay an important foundation for further studies. This subject is useful for the determination of lithostatic pressure changes on rocks in deep depth. The tunnel surrounding environment in the depth of the earth has this condition.

For the evaluation of static and dynamic energy and other mechanical and dynamical properties of rocks, three types of rocks were selected. At first geological properties of samples were evaluated by the geological survey, thin section study, and X-ray analysis. Then cylindrical specimens were prepared according to ASTM D4543 and the required parameters were obtained under various axial and lateral stress conditions according to ISRM. During the tests, an ultrasonic test with both P and S waves was conducted and the wavelet was recorded. Usually, the velocity of P and S waves upon arrival from the specimen are determined for evaluation of dynamic properties of rock specimen. Although this parameter is very useful for the prediction of some static parameters, other parameters could be determined from wavelets that can remark useful information from rock specimens.

2. Energy consumption during the stress path of rock

The energy (work) from a load-displacement diagram is the area under the load-displacement curve. To calculate work (w), it is required to determine the area under the curve of the load with respect to displacement as Eq. (1).

$$\mathrm{w} = \int \mathrm{F.dL} \tag{1}$$

where F is the force/load and dL is the change of specimen length.

In conventional tests, the values of loading and displacement are recorded by the digitized instrument at a selective time duration. So, for the approximate area between every two load-displacement endpoints of the sample (energy absorption), the trapezoidal rule is used as Eq. (2).

$$\text{Energy} = \frac{1}{2}(d_2 - d_1) \times (F_2 + F_1) \tag{2}$$

where d_1 and d_2 are the displacement endpoints at first- and second-time data recording and F1 and F2 are the force/load for the same time (Fig. 1). Finally, by summation of all data ranges, the overall energy absorption is determined.

The total work of the external load is converted to the elastic energy (E_e) accumulated in the testing machine system and the energy U is absorbed by the rock sample due to deformation and failure (Ruidong 2005).

In many projects, rocks didn't fail, but they are deformed. This deformation that occurs by applying force is shown with deformability coefficient (modulus). Common deformability coefficients are tangent or Young's modulus

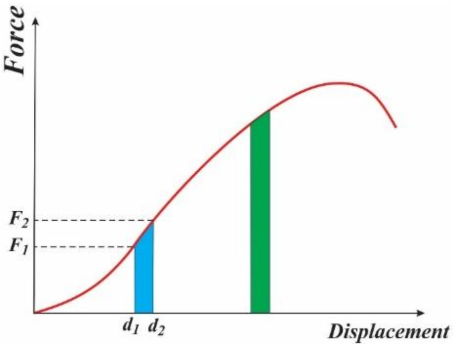

Fig. 1 Energy determined from variation of length sample in selective intervals

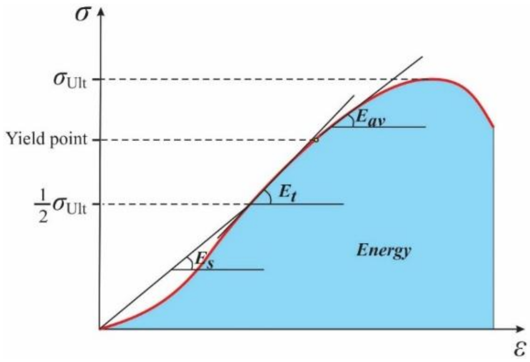

Fig. 2 Energy, Young's modulus (E_t), secant modulus (E_s), and average modulus ($E_{\alpha v}$)

(E_t), secant modulus (E_s), and average modulus ($E_{\alpha v}$) that shown in fig. 2. As shown in this figure, the values of these modules aren't equal and depend on the stress condition on the sample. In the first stage of axial stress, usually, the initial pore in the specimen becomes closed. Then, the specimen has elastic behavior until increased stress reaches the Yield point. After that, the specimen has plastic mode and axial strain is increased. At the failure stage, the stress-strain curve is horizontal. After failure, the slope of stress-strain has come downward.

3. Receiving energy from the pulse wave

3.1 Pulse wave description

In general, two methods of pulse wave are used. In the first method, only receiving wavelet is recognized for the determination of dynamic properties. During the sending and receiving of the wave, a small fluctuation is observed that determines the beginning of test time. After this, some very small fluctuation is observed that imply device noise and suddenly the peak amplitudes appear. The first time that peak amplitudes are observed is the receiving time and therefore, the time arrival is differential between send and receive time (Fig. 3). It must be noted that the time duration of caps should be subtracted from differential time.

The second method for determining of dynamic properties of the sample is the registration of sending and receiving wavelets separately and then put them together to determine the arrival time. At this method, the zero-time is determined when the device is calibrated and the receiving time is a confluence of send and receive wavelet after zero-time (Figs. 4 and 5).

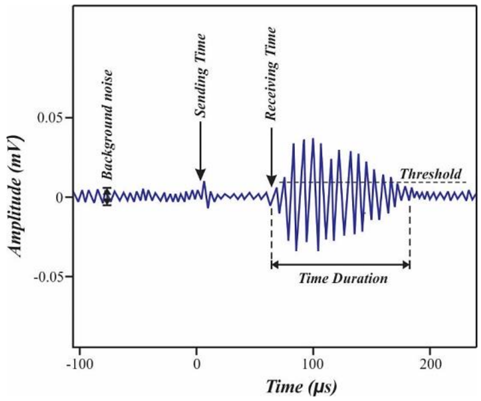

Fig. 3 Wavelet registration from the usual ultrasonic pulse transmission technique

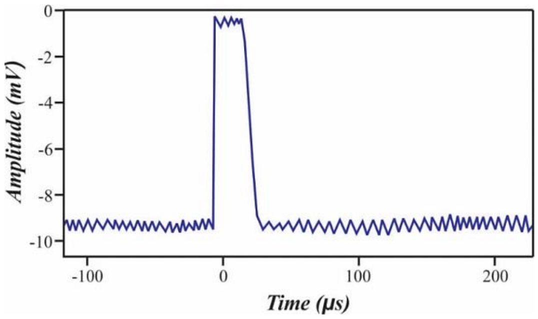

Fig. 4 Wavelet of send

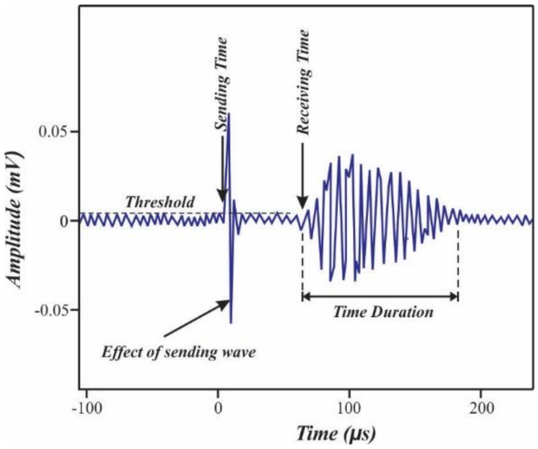

Fig. 5 Wavelet of receive

The amplitudes of waves usually are specified in the logarithmic decibel (dB) scale or millivolt (mV).

3.2 Calculation of wave energy

All surface surrounding between wavelet curve and zero-line of amplitudes in a received wavelet remark returned energy from an acoustic emission (AE) source. This energy depends on AE source energy, the distance between AE source and receiver, materials characteristic that waves passing through, etc.

Usually, the wave energy (E) in term Joule (= watt × second) can be calculated from Eq. (3):

$$E = \frac{1}{2} C.V^2 \tag{3}$$

That C is capacitance (Farad or coulomb per volt) and V is peak voltage in term of Volt. But it should be noted that in this equation, the entire wavelet was not considered and the only peak of the wave has the main role in wave energy.

However, the energy can be calculated in any required duration time. For the determination of pulse receive energy, Xie *et al.* (2011) proposed the surface under the envelope curve shows the energy of wave (Fig. 6). The determined energy by this method has a serious error because the wavelet usually hasn't sympathetic to the

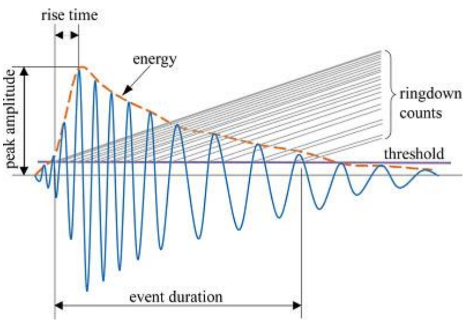

Fig. 6 Features of transient AE waveform (Xie *et al.* 2011)

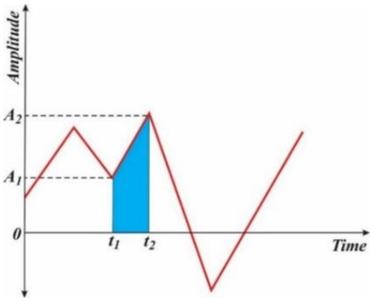

Fig. 7 The area above the horizontal axis

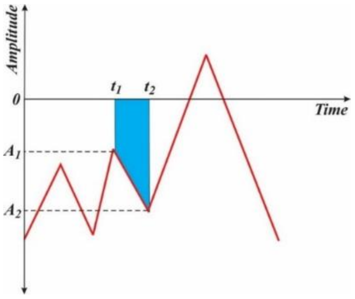

Fig. 8 The area below the horizontal axis

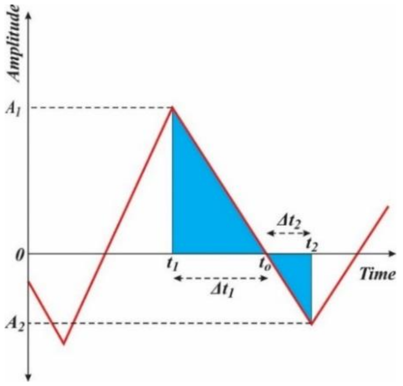

Fig. 9 The area above and below the horizontal axis

horizon axis. In the wavelet graph, the area between the sinusoidal curve and the horizontal axis shows the received energy.

Rock deformation is accompanied by energy release, which can be recorded by AE sensors. The released energy is equal to the sum of the absolute value of the area between the envelope of the signal wave and the threshold line (Li *et al.* 2019). This energy calculation can acquire from wavelet by some equations that bring forward. In this study, derived energy is calculated from P and S waves instead of AE sensors. So, the equipment of AE sensors is not necessary, but the wave energy must be calculated by the following equations.

If the curve of the wavelet was above the zero amplitude line (A1 and A2 >0), the area under wave line (AreaAbove) can be calculated from Eq. (4):

$$\mathrm{Area}_{Above} = \frac{1}{2}(t_2 - t_1) \times (A_2 + A_1) \tag{4}$$

where t_1 and t_2 are the time at the first and second point respectively and A_1 and A_2 imply the amplitude arrival at the first and second time of the wavelet curve.

Also, for the point under the wavelet curve (A_1 and $A_2<0$), the area between wavelet and time axis can be determined from Eq. (5):

$$\mathrm{Area}_{Below} = -\frac{1}{2}(t_2 - t_1) \times (A_2 + A_1) \tag{5}$$

By a combination of Eq. (3) and Eq. (4), the area above and below the horizontal axis ($A_{A\ \&\ B}$) can be calculated from Eq. (6):

$$\mathrm{A}_{A\ \&\ B} = \left|\frac{1}{2}(t_2 - t_1) \times (A_2 + A_1)\right| \tag{6}$$

For the part of the curve that one point is located above the zero horizontal axis (amplitude > 0) and another one is below that axis (amplitude < 0), i.e., multiplication of two numbers are negative ($A_1 \times A_2<0$), so, for determination, the area at first, the location of the point that has zero amplitude in the horizontal axis (time axis) that is t_o should be calculated (Fig. 8). For determination of t_o, Δt_1 must be calculated from Eq. (7):

$$\Delta t_1 = \mathrm{A}_1 \frac{(t_2 - t_1)}{(A_2 + A_1)} \tag{7}$$

So, t_o is determined by Eq. (8):

$$t_o = t_1 + \Delta \mathrm{t}_1 \tag{8}$$

Similarly, Δt_2 is determined from Eq. (9):

$$\Delta t_2 = \mathrm{A}_2 \frac{(t_2 - t_1)}{(A_2 + A_1)} \tag{9}$$

It should be noted that A_1 and A_2 must be positive, so the absolute value of these should be considered.

Finally, the total area for these two recent modes above and below of time axis (A_F) can be calculated from Eq. (10):

$$A_F = \frac{|\mathrm{A}_1|.\Delta t_1}{2} + \frac{|\mathrm{A}_2|.\Delta t_2}{2} \tag{10}$$

With a combination of Eq. (7), Eq. (9), and Eq. (10) total areas between the horizontal axis and wavelet is determined from Eq. (11):

$$A_F = \frac{\mathrm{A}_1{}^2 \frac{(t_2 - t_1)}{(A_2 + A_1)}}{2} + \frac{\mathrm{A}_2{}^2 \frac{(t_2 - t_1)}{(A_2 + A_1)}}{2} \tag{11}$$

where the values of A_1 & A_2 must be absolute value, too.

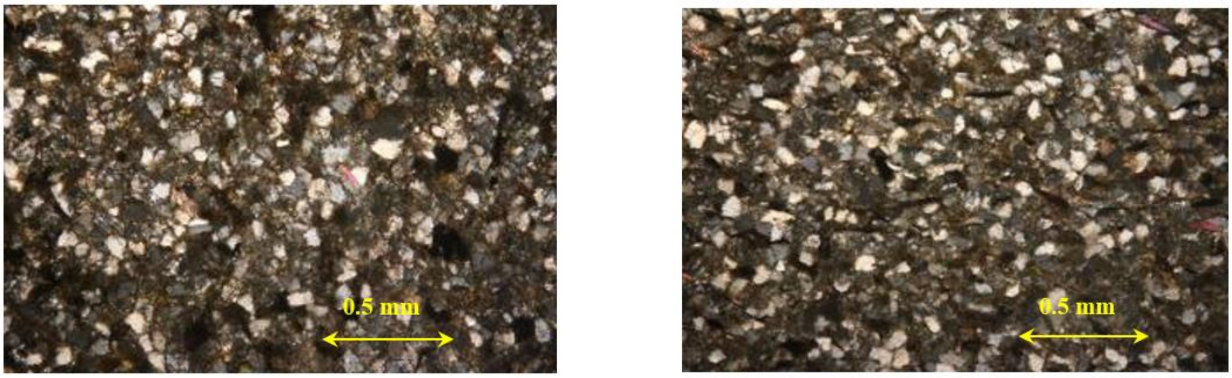

(a) Parallel to bedding (b) Perpendicular

Fig. 10 Thin section of sandstone

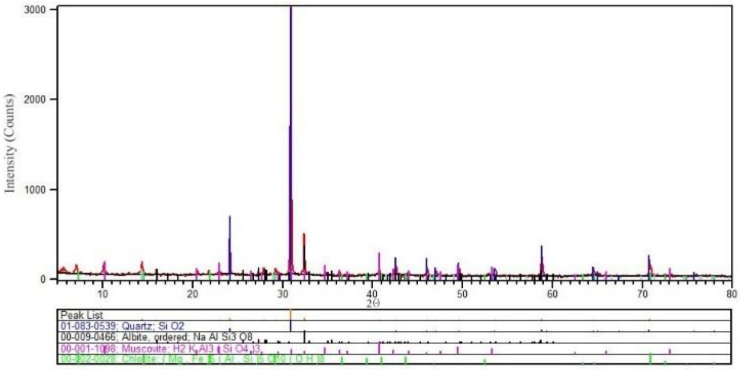

Fig. 11 Mineral identification of sandstone determined by XRD analysis

Table 1 Chemical composition of sandstone rock samples determined by XRF analysis

Compound	Concentration (%)	Compound	Concentration (%)	Compound	Concentration (%)	Compound	Concentration (%)
SiO_2	56.92	Na_2O	2.14	ZrO_2	0.126	Rb_2O	0.019
Al_2O_3	17.00	CaO	1.60	CuO	0.063	Y_2O_3	0.009
Fe_2O_3	14.61	TiO_2	1.14	ZnO	0.059	Nb_2O_5	0.007
K_2O	3.25	MnO	0.468	SO_3	0.040	LOI*	---
MgO	2.20	P_2O_5	0.130	SrO	0.033	Total	99.18

*Loss On Ignition (1000˚C, for 2h)

Then Eq. (11) can show as Eq. (12):

$$A_F = \left(A_1^{\,2} + A_2^{\,2}\right)\frac{(t_2 - t_1)}{2(A_2 + A_1)} \tag{12}$$

Finally, the total energy of the AE (A_t) can be determined by Eq. (13):

$$A_t = A_{A\,\&\,B} + A_F \tag{13}$$

The unit of energy depends on the fluctuation of the voltage domain and time duration between pulse wave received and attenuated.

4. Rock types and test procedure

4.1 Description of rock samples

Three types of rock samples were selected for this study that are sandstone and two types of pyroclastic rocks. For identification and evaluation of these rocks, field survey, handy sample study, thin section study, and X-ray analysis such as XRF (X-Ray Fluorescence) and XRD (X-Ray Diffraction) analysis were done for all of them. The specimens were intact and evidence such as a vein or porous media were not observed on them. The thin sections of the specimen were provided in two directions to the bedding that are parallel and perpendicular for recognition of minerals, sedimentary environment conditions, and isotropy. Also, X-ray analysis was used to determine chemical compositions and mineralogy of specimens by XRF and XRD analysis, respectively.

4.1.1 Sandstone sample

The sandstone rock has a gray color and clastic grains. The bedding of this rock has 20 to 30 cm thickness and vein futures, crack and discontinuities plane weren't seen in the

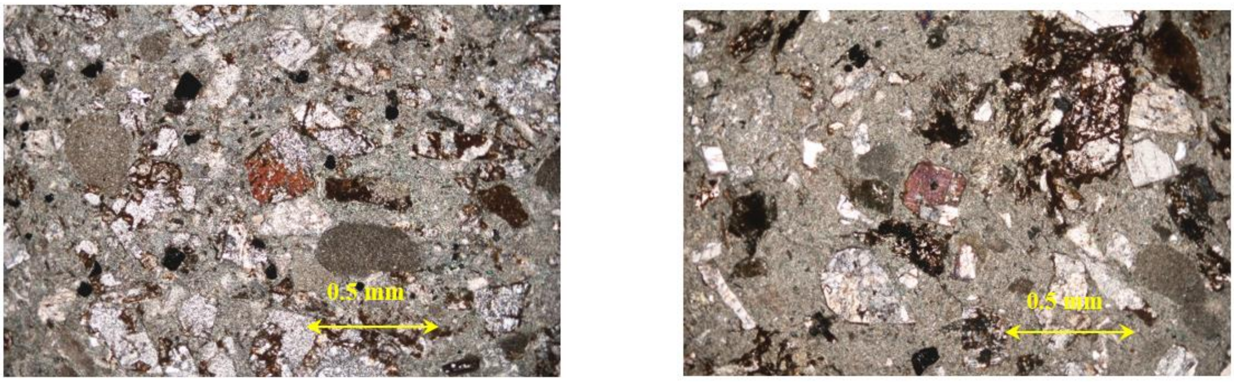

(a) Parallel to bedding (b) Perpendicular

Fig. 12 Thin section of pyroclastic rock

Table 2 Chemical composition of pyroclastic rock samples determined by XRF analysis

Compound	Concentration (%)	Compound	Concentration (%)	Compound	Concentration (%)	Compound	Concentration (%)
SiO_2	59.2	MgO	1.36	BaO	0.051	Rb_2O	0.011
Al_2O_3	15.3	TiO_2	0.629	MnO	0.037	ZnO	0.01
CaO	6.93	P_2O_5	0.12	SrO	0.033	Y_2O_3	0.004
Fe_2O_3	3.68	SO_3	0.078	CuO	0.018	LOI*	7.14
K_2O	2.84	Cl	0.053	ZrO_2	0.016	Total	99.85
Na_2O	2.34						

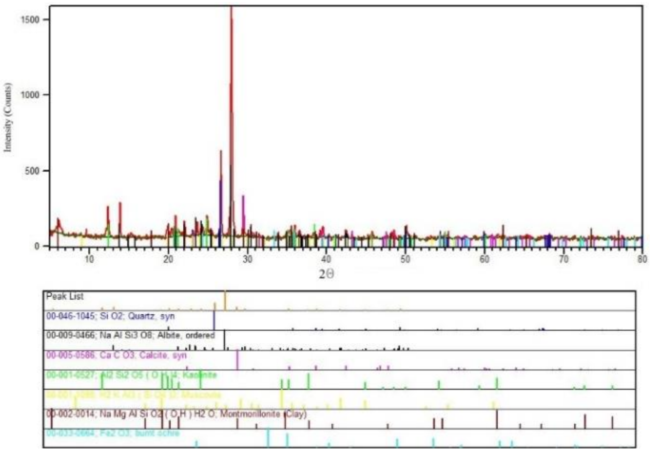

Fig. 13 Mineral identification of pyroclastic rock determined by XRD analysis

cylindrical samples by necked eye. The rock samples seem to be isotropic and homogenous.

The rock used in the laboratory test was medium-grained and is relatively isotropic in texture and composition. Figs. 10(a) and 10(b) shows the thin section of the rock sample in parallel and perpendicular to bedding, respectively. The grading of minerals in both directions shows the gentle and continuous deposit in the sedimentary environment and rock has almost homogeneity.

According to Fig. 10, the average grain size of minerals is about 0.1 mm and are mostly good sorted and weakly rounded quartz. Some rock fragments and little chlorite and albite that appear with the slight alteration of feldspars are seen in the sample's thin section. The absence of minerals elongation within the matrix of rock is remarkable. However, the washing of clay minerals in the rock was negligible.

The chemical composition of samples was determined by XRF and minerals identification by thin section and XRD analysis, which is shown in Table 1 and Fig. 11 respectively.

The XRF result that was examined on the powder sample of rocks (Table 1) show that SiO_2, Al_2O_3, and Fe_2O_3 compose most of the composition of the rock.

The minerals that are recognized by XRD analysis (Fig. 11) were quartz, albite, muscovite, and chlorite.

According to Pettijohn *et al.* (1971) classification system, feldspathic greywacke sandstone has the best corresponding name for this rock.

4.1.2 Pyroclastic sample

The two pyroclastic rock specimens are almost similar.

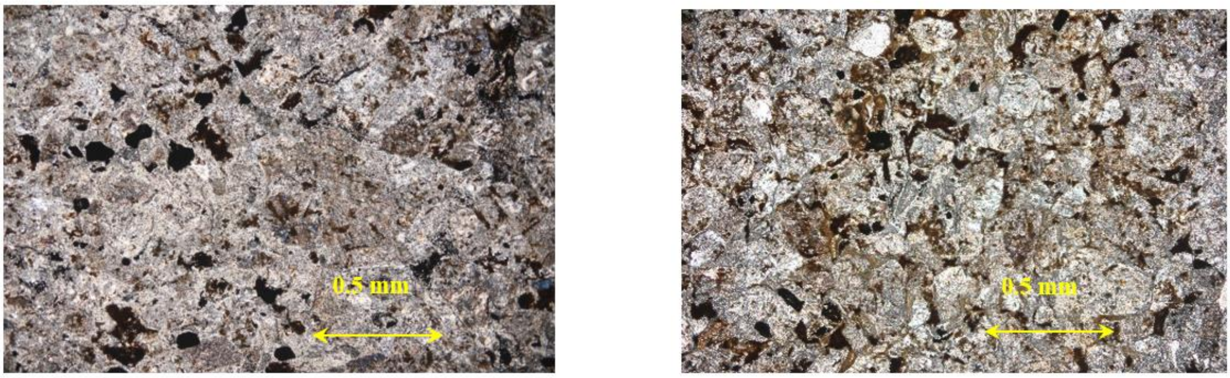

(a) Parallel to bedding (b) Perpendicular

Fig. 14 Thin section of argillitic tuff

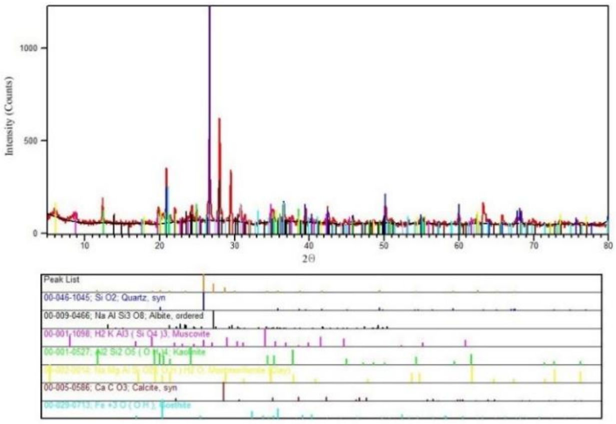

Fig. 15 Mineral identification of argillitic tuff determined by XRD analysis

Table 3 Chemical composition of argillitic tuff determined by XRF analysis

Compound	Concentration (%)	Compound	Concentration (%)	Compound	Concentration (%)	Compound	Concentration (%)
SiO_2	52.2	Na_2O	2.32	MnO	0.102	ZnO	0.012
Al_2O_3	19.3	MgO	1.24	Cl	0.065	Rb_2O	0.005
CaO	6.6	TiO_2	0.727	SrO	0.021	Y_2O_3	0.004
Fe_2O_3	4.02	SO_3	0.214	ZrO_2	0.018	LOI^*	10.44
K_2O	2.43	P_2O_5	0.13	CuO	0.018	Total	99.87

The result of the XRF and XRD test are shown in Table 3 and Fig. 15, respectively.

They have a green color and clastic grains. The bedding of rocks at the sampling site has various thickness between less than 5 centimeters up to 1 meter. These samples were obtained from a layer with 20 cm thickness and samples have no apparent weak plane and seem to be almost isotropic. The rock specimens coring was obtained perpendicular to bedding.

The volcanic clasts, pyroxene, chert, and opaque minerals are seen in a thin section of these rocks. The biotite and hematite are also found in the rock. The grain size of minerals varies and reaches up to about 4 millimeters. Figs. 12(a) and 12(b) shows the thin section of the rock sample in parallel and perpendicular to bedding, respectively. The rock has poor sorting and the grains are angular.

The alteration of minerals such as feldspars has led to the appearance of calcite, biotite, and hematite in their margins. The silica cement is connected to the grains. The goethite and clay minerals are also found in the rock. The result of the XRF and XRD test of the sample are shown in Table 2 and Fig. 13, respectively.

According to the pyroclastic classification Gillespie and Styles (1991), this rock seems to be a Lapilli-tuff stone.

4.1.3 Argillitic pyroclastic sample

The pyroclastic light brown color specimen showed slight bedding in the handy scale. The rock specimen coring was obtained perpendicular to bedding. The grains have moderate roundness with an average size of 0.15 mm (Fig. 14(a) and 14(b)). The clayey matrix filled the pore spaces between the poor sorting grains in the rocks. The quartz, calcite, albite, kaolinite, muscovite, montmorillonite, and

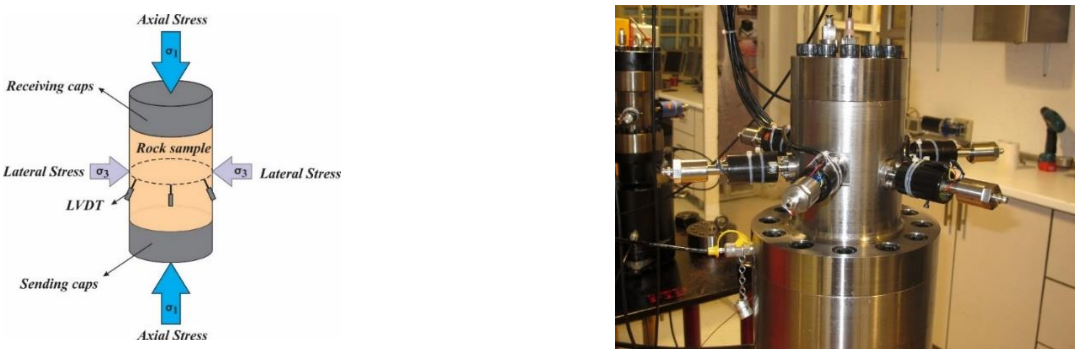

(a) Rock sample and location of lateral LVDT (b) Distributions of lateral extensometers

Fig. 16 Triaxial compression test

goethite are the dominant minerals (Fig. 15). The rock according to the classification of pyroclastic rocks (Gillespie and Styles 1999) is called tuff.

4.2 Test procedures

The triaxial compression tests were carried out using a computer-controlled servo-controlled hydraulic compression system which mainly consists of a testing machine, hydraulic power supply, triaxial cell, and digital controller. The system has a maximum axial load capacity of 500 kN, can supply a maximum confining stress of 70 MPa (700 bar). The accuracy of confining pressure was 0.01 bar. Also, for relative comparison of accuracy and validity of digital cell pressure, analog gage values were recorded during the time test, too. This triaxial machine is specified for the specimen with 38 mm diameter and length to diameter ratio (L/D) of 1.5 to 3.

The axial and lateral strains of the sample during loading were acquired automatically by the extensometers. A single extensometer was used for registering axial strains and for lateral strain, 6 extensometers were used. Using 6 extensometers for lateral deformations is useful for the determination of anisotropy of the rock sample during loading. The axial and lateral extensometers have 0.001 mm accuracy.

For evaluation of the relation between wave velocity and wave energy in rocks at various axial and lateral pressure, the rock sample was tested with the triaxial servo-controlled machine. The axial and lateral pressures were recorded at every second of the test duration. To determine the strain value, axial and lateral displacements of the sample were recorded by LVDT (Linear Variable Differential Transducer). For the recording of lateral strain, 6 LVDT's that are shown in Figs. 16(a) and 16(b) were used.

Before testing, some physical and ultrasonic properties of rock samples were determined in the ambient environment. Then, the sample was placed in triaxial conditions. Then the sample was under a little pressure until the axial and lateral pressures were fixed. After this stage, axial and lateral loadings were increased as axial stress was greater than lateral stress during all test processes. At the initial loading stage, axial load-controlled loading was used with a loading rate of 0.01 mm/min. The test was conducted according to ISRM (1983) standard test method. The triaxial test method of rock based on ISRM can be executed in 3 methods. In this complicated study, type II of this standard test method that is used to test the rock in multi-stages was selected, but in all stages, lateral pressure is fixed and axial stresses are increased (as a fixed strain) to the defined pressure and then the lateral pressure is increased to higher pressure and the test will be continued based on strain control to the next defined axial pressure. For example, when the stress is reached 50 MPa, the loading mode control was switched from axial load control to axial deformation control at a constant rate of 0.01 mm/min under confined conditions till to 100 MPa axial stress and so on. These stages are continued until the stress-strain behavior of the specimen was almost elastic. The triaxial test of rock specimens was done under 5, 10, 15, and 20 MPa confining pressure stages.

With the beginning of increasing deformability of the sample due to the excess axial loading, loading is stopped, and then gradually the axial load is decreased and It reached close to zero. Then the lateral stress increases and the next step of the test start.

At the end stage of every axial loading, both P and S wavelets are send and received. By determination of P and S waves' velocity, both send and receive waves are matched. Thus, the zero-time, delay time for traveling waves inside of two caps, and time of passing through the rock specimen are determined. The wave frequency for all ultrasonic tests were 1.7 MHz.

For the determination of energy calculated, at first, the sending energy is evaluated and then the received energy is calculated. However, if the sending energy for each separate test was equal to changes in received energy are due to events occurring on the route of specimen. So, in this study, these variable energies are the result of the different stress conditions applied to the sample.

The cores with a diameter of about 38 mm were taken from rock blocks for the servo-controlled triaxial test with ultrasonic test synchronized. The sampling blocks were taken from the surface and specimen coring were perpendicular to bedding.

The length of the samples was almost twice their diameter. The tolerance of perpendicularity and flatness of the specimens met the specifications of the ISRM suggested method (Fairhurst and Hudson 1999). In particular, the ends of all the specimens were carefully polished to minimize the end effect during loading.

5. Test result

5.1 Stress-strain

The stress-strain curves of all specimen are shown in Figs. 17-20. Note that, the lateral strain is corrected to zero at the start of each step of axial loading with increasing lateral stress. The pyroclastic rocks (S1 and S4) have similar ultimate strength at 20 MPa lateral stress, axial and lateral deformation till failure. The argillitic pyroclastic has the maximum deformation to failure. Also, this specimen has a lower strength between samples. Altogether the sandstone specimen failure occurs at 15 MPa lateral stress, but the axial stress was about 258 MPa at that condition. So, the sandstone had shown greater strength compared to other specimens.

According to the stress-strain curve of samples, the slope of axial stress – lateral strain curve at a higher value of lateral stress are greater than lower lateral stress. Also, the higher lateral stresses cause the lateral strain of the specimen to be reduced, but the axial stress – lateral strain curve at higher lateral stress has a steep slope.

Fig. 21 shows the specimens after failure in the triaxial test. According to the mineralogy of specimens, predicted that sandstone that has quartz in its composition has the most strength. On the other side, argillitic pyroclastic rock with clay minerals has less strength compared to others. Although the pyroclastic rock (S1 and S4 specimens) have high strength, the range of it is between sandstone and argillitic pyroclastic specimens.

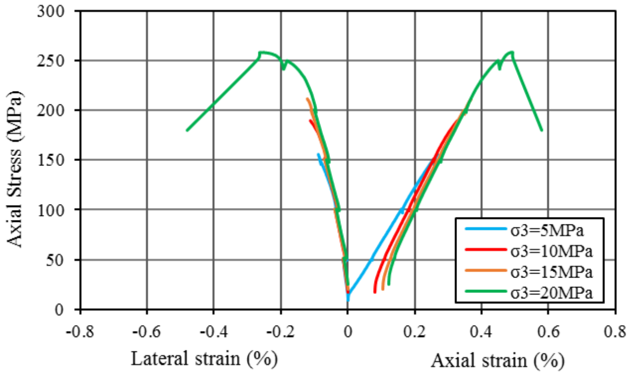

Fig. 17 The stress-strain curve of pyroclastic (S1) in multistage triaxial test

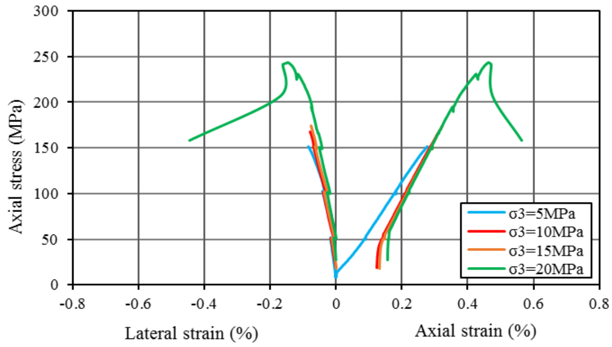

Fig. 18 The stress-strain curve of pyroclastic (S4) in multistage triaxial test

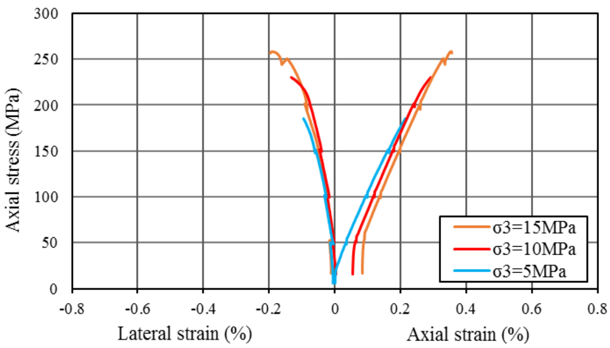

Fig. 19 The stress-strain curve of sandstone (S5) in multistage triaxial test

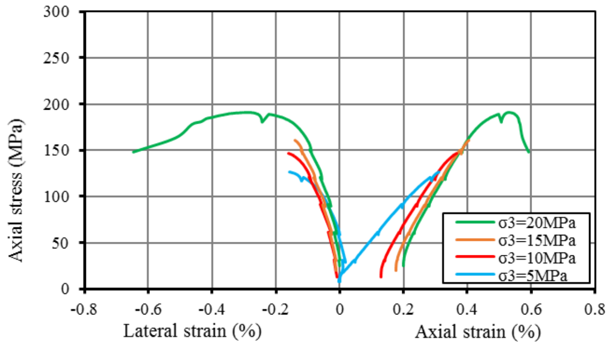

Fig. 20 The stress-strain curve of argillitic pyroclastic (5E) in multistage triaxial test

S1 S4 S5 E5

Fig. 21 The specimens after failure in the triaxial test: S1 and S4: Pyroclastic, S5: sandstone, and 5E: argillitic tuff

5.2 Wave velocity

The P wave velocities of samples (V_P) during axial and lateral stress are shown in Figs. 22(a)-22(d). Generally, with increasing axial pressure on the sample, the p-wave velocity increases. The increased lateral pressure should also increase the velocity of the wave in the samples, however, since the incremental increase in the range of lateral pressure is less than the axial pressure, its effect on the graphs is not visible.

The value of V_P for sandstone specimen (Fig 22(c), S5)

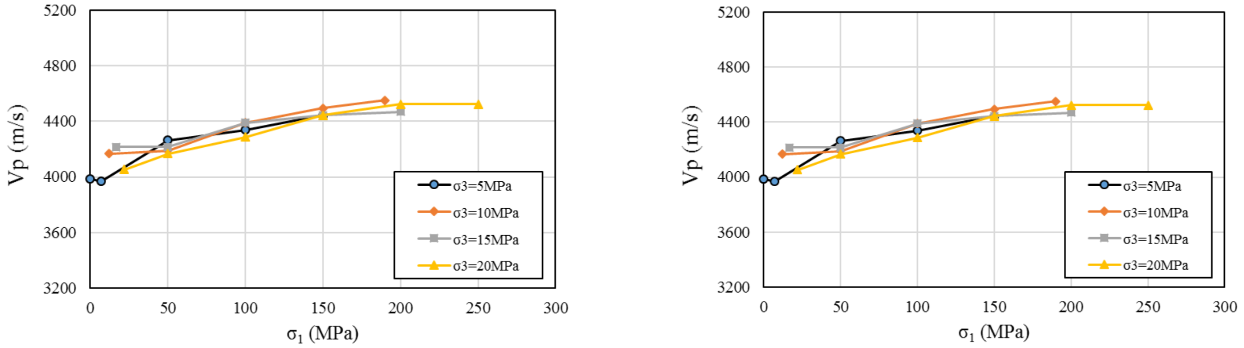

(a) V_P versus $σ_1$ in the S1 spesimen (b) V_P versus $σ_1$ in the S4 spesimen

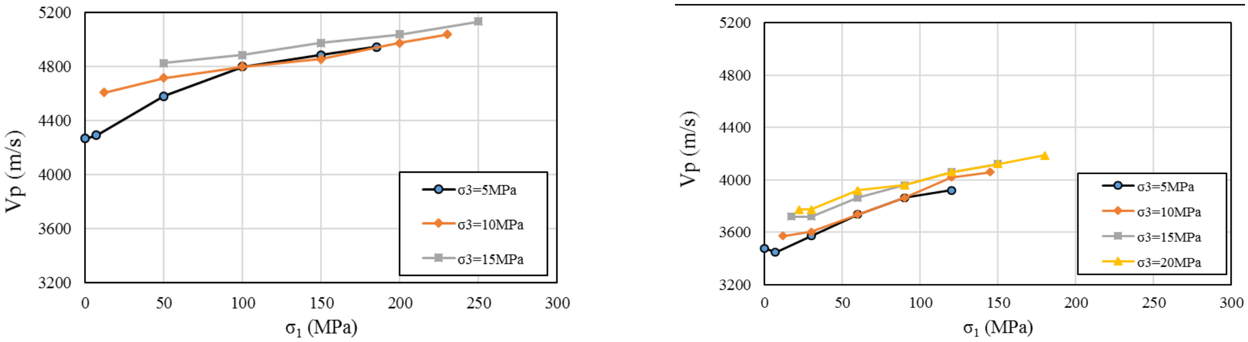

(c) V_P versus $σ_1$ in the S5 spesimen (d) V_P versus $σ_1$ in the 5E spesimen

Fig. 22 The relation between P wave velocity (V_P) and axial stress in various lateral stress

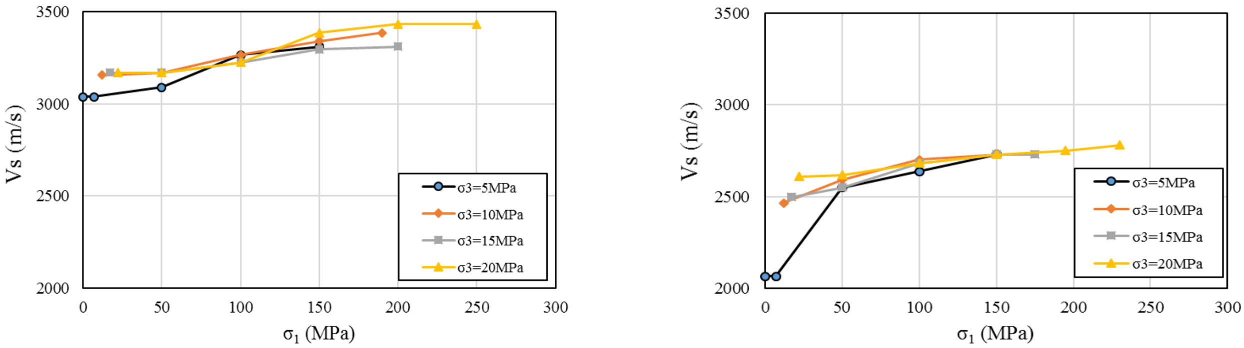

(a) V_S versus $σ_1$ in the S1 spesimen (b) V_S versus $σ_1$ in the S4 spesimen

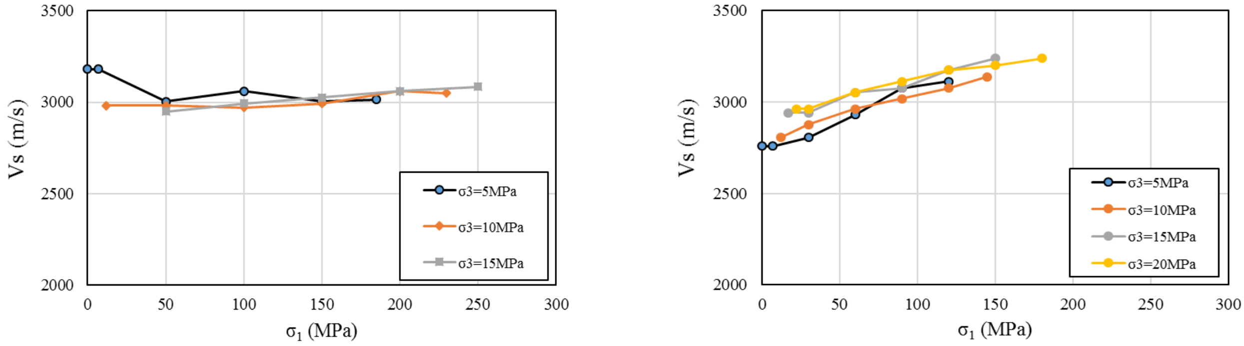

(c) V_S versus $σ_1$ in the S5 spesimen (d) V_S versus $σ_1$ in the 5E spesimen

Fig. 23 The relation between S wave velocity (V_S) and axial stress in various lateral stress

is more than other. The Vp of sandstone specimen (S5) at high value of axial stresses can exceed 5000 m/s. This subject is matched with static strength of them which sandstone specimen has the most strength. The two specimens of S1 and S4, which had almost the same conditions in terms of mechanical strength, have approximately the same values of longitudinal wave velocity in the corresponding values of axial and lateral pressures. In general, the values of longitudinal wave velocity in them is less than the sandstone specimen (S5) and more than the clay pyroclastic sample (5E). The argillitic pyroclastic specimen (5E) has a lower value of V_P

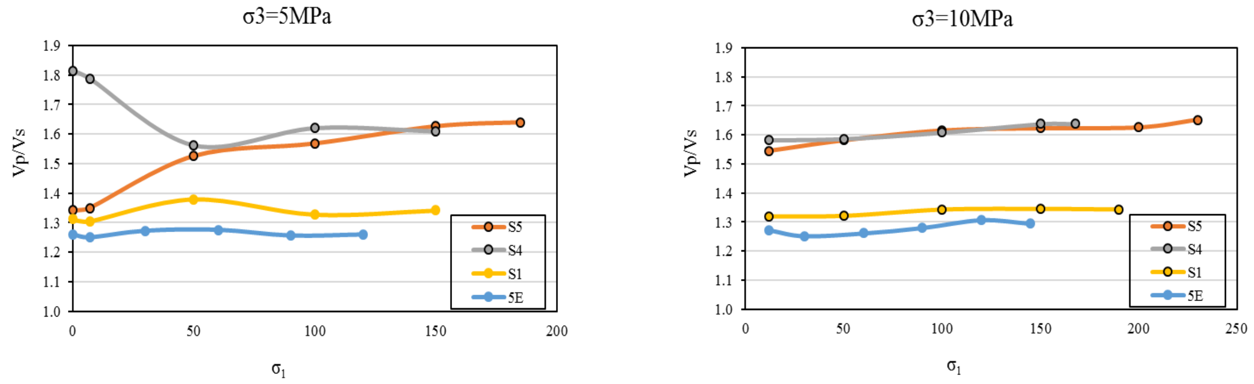

(a) V_P/V_S in σ_3=5MPa for all specimens

(b) V_P/V_S in σ_3=10MPa for all specimens

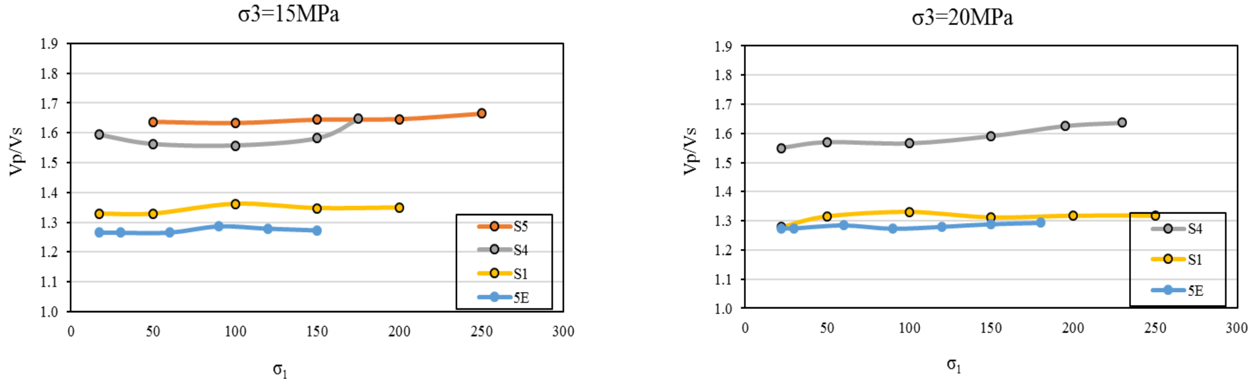

(c) V_P/V_S in σ_3=15MPa for all specimens

(d) V_P/V_S in σ_3=20MPa for all specimens

Fig. 24 The V_P/V_S ratio in various axial and lateral stresses

and less strength.

The S wave velocity of samples (V_S) during axial and lateral stress is shown in Figs. 23(a)-23(d). Although with increasing axial stress, S wave velocities were increased, the trend and relation between increasing axial and lateral stress on the S wave velocity of samples are not as well as P wave velocity.

The sandstone sample (S5) has the most anomalies in V_S values in the specimens. At the first stage of axial loading, maybe decreasing the S wave velocities with increasing the axial pressure in that specimen is related to the appearance of new cracks. The V_s values in the sandstone specimen were almost constant. Perhaps the compressibility and high strength of this specimen cause this phenomenon.

The V_P/V_S ratio at various axial and lateral stresses in all specimens show in Figs. 24(a)-24(d). The value of V_P/V_S for strength specimen (sandstone) is higher and for the weakest specimen (argillitic specimen, 5E) has less value.

Although using of wave velocity is useful for evaluating the mechanical and dynamic properties of rocks, but the presence of some unexpected conditions such as the occurrence of cracks or small cavities when loading on rocks causes anomalies in the predicted process of axial and lateral stresses on the rock specimen. One of the major chalenge of using wave velocity to investigate the dynamic properties is to calculate the passage time of the wave. Because in many cases, receiving time measurement of the first wave peak can be associated with the error. Although the accuracy of measuring time and wave oscillation by an ultrasonic device can solve this problem to some extent, but for more accurate work, sometimes this problem is still observed.

5.3 Static and dynamic energies

The use of wave energy can improve the trend of changes in pressures on the rock sample more than the wave velocity. Because in the wave energy, all the data of the wave graph (wavelet) are considered and the problem of calculating the wave velocity, which is related to the time of receiving its first peak, is solved (Heidari *et al.* 2020).

For the calculation of static and dynamic energies, Eq. (2)-(13) were used, respectively. The static energy was calculated from the area that involves 0.005 percentage of strain data cumulated from axial loading before reaching the desired axial stress. Since this method provides the accuracy of the machine for a uniform rating of increasing stresses during the test, the calculation of the area was conducted based on the distinct displacement. For the specimens with plastic behavior, after their elastic behavior ends (yield point), the deviator from the straight line will appear. The dynamic energy was calculated from the first point of receiving wavelet to the last data registered. The total data of every pulse wavelet was 5000 points involve time (μs) and amplitude (mv). For the determination of pulse wave return energy, only about 3500 data numbers that were located after the first point of the received wave were used. Due to the difficulty and time consuming processes of wave energy calculations by the computer, this amount of data has been taken into account for this research. Obviously, increasing the number of data in wavelet, which is determined by the accuracy of the

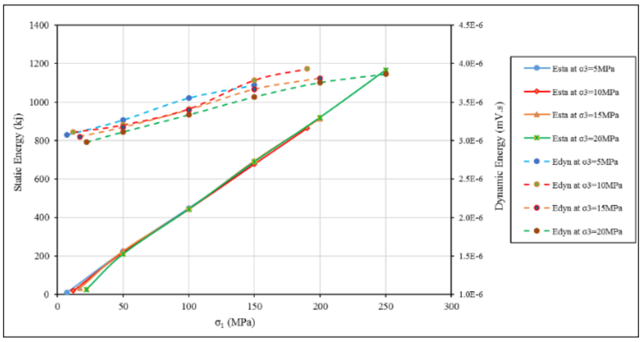

Fig. 25 The relation between static energy (E_{sta}) and dynamic energy (E_{dyn}) in pyroclastic (S1)

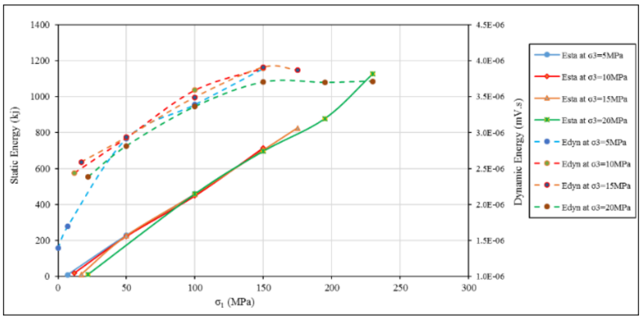

Fig. 26 The relation between static energy (E_{sta}) an dynamic energy (E_{dyn}) in pyroclastic (S4)

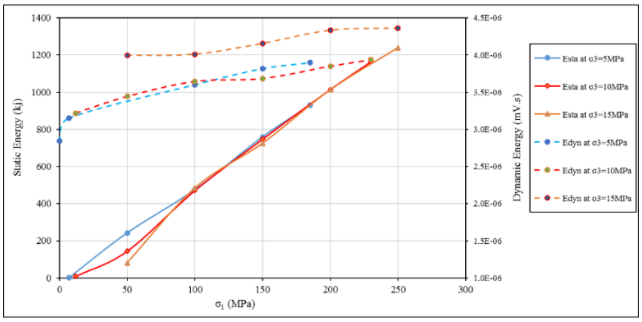

Fig. 27 The relation between static energy (E_{sta}) and dynamic energy (E_{dyn}) in sandstone (S5)

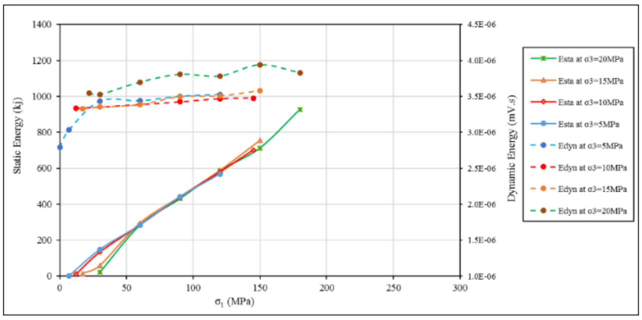

Fig. 28 The relation between static energy (E_{sta}) and dynamic energy (E_{dyn}) in argillitic pyroclastic rock (5E)

ultrasonic device, can increase the time of calculations. However, the use of this amount of data was appropriate for this study.

Figs. 25-28 show the comparison between static energy (E_{sta}) and dynamic energy (E_{dyn}). Static energy is related to the stiffness of rocks. The rocks with higher strength and Young's modulus have more static energy. In this study, sandstone has the highest strength and Young's modulus, so for its deformation, more energy was used compared to other rocks. The argillitic specimen that has the least strength and Young's modulus, required the minimum energy for deformation compared to other rocks.

According to these graphs, the dynamic energy increases with the increase of axial stress, and the increases of lateral stresses reduce the dynamic energy at the same axial stress. Li *et al.* (2019) found that in the triaxial test of salt rock under confining pressures of 5, 10, 15, and 20 MPa, the higher confining pressure shows few AE events. The results reflected that the confining pressure had an inhibitory effect on AE activity. The relationship between confining pressure and AE activity has been also studied previously by Ai *et al.* (2011) which shows that the confining pressure can effects AE activity during the failure process in coal specimen under triaxial test.

As are shown in Figs. 26 to 29, the returned pulse energy is varied under different confining pressures (5, 10, 15, or 20 MPa). This finding is similar to the results of other experimental tests based on AE events. It must be noted that, with increases of lateral pressure at a distinct axial pressure, the amount of return energy of the wave would also decrease. This is not always true. Perhaps, it may be due to the rock mineralogy or the orientation of anisotropic minerals. The texture and fabric of the specimen could increase the returning energy of the wave with increasing lateral pressure. The arising of returning energy with increasing lateral stresses was clearly visible in the argillitic specimen (5E). Perhaps, the compressibility and deformability of clay minerals without fracturing during loading have the main roles for a direct relationship between increasing the pulse return energy and lateral stress. This feature in clayey rocks can also be effective in low lateral pressures such as 5, 10 or 15 MPa.

6. Conclusions

In this study, the geological, mechanical, and dynamic properties of some rock specimens were evaluated. To compare the mechanical and dynamic properties of four specimens in various conditions of axial and lateral stresses, they were tested by a servo-controlled triaxial machine. However, the statistical analysis was not the focus of this study.

The main objective of this study was to determine the relationship between the static and dynamic energy of specimens under various axial and lateral stress. According to the longitudinal wave velocity and stress-strain diagrams of the specinems, it can be acknowledged that there is a great relationship between changes in mechanical properties and wave velocity in rocks. The results indicated that the increase of static and dynamic energy (returned pulse wave energy) due to rising axial stresses are visible in all specimens, but the effect of lateral stress on the increase or decrease of returned pulse energy at similar static energy depends on fabric and texture of rocks. Thus, it could lay a foundation for the quantitative evaluation of the stress in rocks. To evaluate the stress changes in the specimen, using the return pulse energy of the wave is more precious and reliable in comparison to wave velocity.

According to the obtained results, the returned pulse wave energy (E_{dyn}) of the specimen is related to their strength of applied static energy. Sandstone which has the most strength has the highest pulse return energy. The amount of Edyn depends on axial and lateral pressures and geotechnical properties of the specimen and could be variable. The range of values in argillic pyroclastic rock is more limited compared to other specimens. This could be related to the geological engineering properties of that rock.

It is worth noting that, the calculated energy could also be related to some other parameters such as the quality of the device used (stiffness of the machine), the intensity of the sending wave, the dimensions of the sample, the assumed range for calculating the returning wave energy, and so on. Therefore, the obtained results on the fluctuation of pulse wave return energy not only depends on the type and characteristics of the rock but also it is related to the characteristics of the mechanical and the ultrasonic devices used.

Acknowledgments

The authors are fully acknowledged the University of Isfahan for supporting financially and the FAN consulting engineering group in Tehran, Iran for providing conditions to perform the triaxial test.

References

Ai, T., Zhang, R., Liu, J.F., Zhao X.P. and Ren, L. (2011), “Space-time evolution rules of acoustic emission locations under triaxial compression”, *J. China Coal Soc*., **36**, 2048-2057.

ASTM D4543 (2008), Standard practices for preparing rock core specimens and determining dimensional and shape tolerances, American Society for Testing and Materials, West Conshohocken, Pennsylvania, U.S.A.

Aydin, A. (2014), “Upgraded ISRM suggested method for determining sound velocity by ultrasonic pulse transmission technique”, *Rock Mech. Rock Eng*., **47**(1), 255-259. https://doi.org/10.1007/978-3-319-07713-0_6.

Cai, M., Kaiser, P.K., Morioka, H., Minami, M., Maejima, T., Tasaka, Y. and Kurose, H. (2007), “FLAC/PFC coupled numerical simulation of AE in large-scale underground excavations”, *Int. J. Rock Mech. Min. Sci*., **44**(4), 550-564. https://doi.org/10.1016/j.ijrmms.2006.09.013.

Chang, S.H. and Lee, C.I. (2004), “Estimation of cracking and damage mechanisms in rock under triaxial compression by moment tensor analysis of acoustic emission”, *Int. J. Rock Mech. Min. Sci*., **41**(7), 1069-1086. https://doi.org/10.1016/j.ijrmms.2004.04.006.

Eringen, A.C. (1980), *Mechanics of Continua*, (2nd Edition), R.E. Krieger, New York, U.S.A.

Fairhurst, E.C. and Hudson, J.A. (1999), “Draft ISRM suggested method for the complete stress-strain curve for intact rock in uniaxial compression”, *Int. J. Rock Mech. Min. Sci. Geomech. Abstr*., **36**(3), 281-289.

Fereidooni, D. (2018), “Assessing the effects of mineral content and porosity on ultrasonic wave velocity”, *Geomech. Eng*., **14**(4), 399-406. https://doi.org/10.12989/gae.2018.14.4.399.

Gillespie, M.R. and Styles, M.T. (1991), “Classification of igneous rocks”, British Geological Survey Research Report, RR 9-06. BGS Rock Classification Scheme.

He, M.C., Miao, J.L. and Feng, J.L. (2010), “Rock burst process of limestone and its acoustic emission characteristics under true-triaxial unloading conditions”, *Int. J. Rock Mech. Min. Sci*., **47**(2), 286-298. https://doi.org/10.1016/j.ijrmms.2009.09.003.

Heidari, M., Ajalloeian, R., Ghazifard, A. and Hashemi, M. (2020), “Evaluation of P and S wave velocities and their return energy of rock specimen at various lateral and axial stresses”, *Geotech. Geol. Eng*., **38**, 3253-3270. https://doi.org/10.1007/s10706-020-01221-9.

Ishida, T., Labuz, J.F., Manthei, G., Meredith, P.G., Nasseri, M.H.B., Shin, K., Yokoyama, T. and Zang, A. (2017), “ISRM Suggested method for laboratory acoustic emission monitoring”, *Rock Mech. Rock Eng*., **50**(3), 665-674. https://doi.org/10.1007/s00603-016-1165-z.

Jaeger, J.C., Cook, N.G.W. and Zimmerman, R.W. (2007), *Fundamentals of Rock Mechanics*, 4th Edition, Blackwell, Singapore.

Koerner, R.M., McCabe, W.M. and Lord, A.E. (1981), *Acoustic Emission Behavior and Monitoring of Soils*, in *Acoustic Emissions in Geotechnical Engineering Practice*, ASTM International, West Conshohocken, Pennsylvania, U.S.A., 93-141.

Kong, X., Wang, E., He, X., Liu, X., Li, D. and Liu, Q. (2018), “Cracks evolution and multifractal of acoustic emission energy during coal loading”, *Geomech. Eng*., **14**(2), 107-113. https://doi.org/10.12989/ae.2018.14.2.107.

Lama R.D. and Vutukuri, V.S. (1978), *Handbook on Mechanical Properties of Rocks*, Vol. 2, Trans Tech, Herzberg, Switzerland.

Li, H., Dong, Z., Ouyang, Z., Liu, B., Yuan, W. and Yin, H. (2019), “Experimental investigation on the deformability, ultrasonic wave propagation and acoustic emission of rock salt under triaxial compression”, *Appl. Sci*., **9**(4), 635. https://doi.org/10.3390/app9040635.

Li, H., Dong, Z., Yang, Y., Liu, B., Chen, M. and Jing, W. (2018), “Experimental study of damage development in salt rock under uniaxial stress using ultrasonic velocity and acoustic emissions”, *Appl. Sci*., **8**(4), 552-565. https://doi.org/10.3390/app8040553.

Lockner, D. (1993), “The role of acoustic emission in the study of rock fracture”, *Int. J. Rock Mech. Min. Sci. Geomech. Abstr*., **30**(7), 883-899. https://doi.org/10.1016/0148-9062(93)90041-B.

Lu, X.B. and Wu, J.Y. (2016), *Theory and Application of Impact Elastic Wave*, China Water and Power Press, Beijing, China.

Martinez-Martinez, j., Benavente, D. and Garcia-del-Cura, M. (2012), “Comparison of the static and dynamic elastic modulus in carbonate rocks”, *B. Eng. Geol. Environ*., **71**(2), 263-268. https://doi.org/10.1007/s10064-011-0399-y.

Mlakar, V., Hassani, F.P. and Momayez, M. (1994), “Crack development and acoustic emission in potash rock”, *Int. J. Rock Mech. Min. Sci. Geomech. Abstr*., **30**(3), 305-319. https://doi.org/10.1016/0148-9062(93)92732-6.

Moradian, Z.A., Ballivy, G., Rivard, P., Gravel, C. and Rousseau, B. (2010), “Evaluating damage during shear tests of rock joints using acoustic emissions”, *Int. J. Rock Mech. Min. Sci*., **47**(4), 590-598. https://doi.org/10.1016/j.ijrmms.2010.01.004.

Najibi, A.R., Ghafoori, M. and Lashkaripour, G.R. (2015), “Empirical relations between strength and static and dynamic elastic properties of Asmari and Sarvak limestones: Two main oil reservoirs in Iran”, *J. Petrol. Sci. Eng*., **126**, 78-82. https://doi.org/10.1016/j.petrol.2014.12.010.

Pettijohn, F.J., Potter, P.E. and Siever, R. (1972), *Sand and Sandstone*, Springer-Verlag, Inc., New York, U.S.A., 618.

Ruidong, P.X.X. (2005), "Effect of elastic accumulation energy of testing machine on the mechanical measurement of rocks", *Mech. Eng.*, **27**(3), 51-55. https://doi.org/10.6052/1000-0992-2004-438.

Sun, X., Hardy Jr, H.R. and Rao, M.V.M.S. (1991*), Acoustic Emission Monitoring and Analysis Procedures Utilized during Deformation Studies on Geologic Materials,* in *Acoustic Emission: Current Practice and Future Directions*, ATSM International, West Conshohocken, Pennsylvania, U.S.A.

Xie, H.L. (2009), "Energy analysis and criteria for structural failure of rocks", *J. Rock Mech. Geotech. Eng.*, **1**, 11-20. https://doi.org/10.3724/sp.j.1235.2009.00011.

Xie, H.P., Liu, J.F., Ju, Y., Li, J. and Xie, L.Z. (2011), "Fractal property of spatial distribution of acoustic emissions during the failure process of bedded rock salt", *Int. J. Rock Mech. Min. Sci.*, **48**(8), 1344-1351. https://doi.org/10.1016/j.ijrmms.2011.09.014.

Zhao, X.G., Wang, J., Ma, L.K., Su, R., Cai, M. and Wang, G.B. (2013), "Acoustic emission behaviors of the Beishan granite under uniaxial and triaxial compression conditions", *Proceedings of the 3rd ISRM SINOROCK 2013 Symposium*, Shanghai, China, June.

CC